

Cosmic web alignments with the shape, angular momentum and peculiar velocities of dark matter halos

Jaime E. Forero-Romero¹, Sergio Contreras^{2,3}, Nelson Padilla^{2,3,4}

¹*Departamento de Física, Universidad de los Andes, Cra. 1 No. 18A-10, Edificio Ip, Bogotá, Colombia*

²*Instituto de Astrofísica, Pontificia Universidad Católica, Av. Vicuña Mackenna 4860, Santiago, Chile*

³*Centro de Astro-Ingeniería, Pontificia Universidad Católica, Av. Vicuña Mackenna 4860, Santiago, Chile*

⁴*Max Planck Institut für Astrophysik, Postfach 1317, D-85741, Garching, Germany*

6 May 2014

ABSTRACT

We study the alignment of dark matter halos with the cosmic web characterized by the tidal and velocity shear fields. We focus on the alignment of their shape, angular momentum and peculiar velocities. We use a cosmological N-body simulation that allows to study dark matter halos spanning almost five orders of magnitude in mass (10^9 - 10^{14}) $h^{-1}M_{\odot}$ and use spatial scales of $(0.5$ - $1.0)h^{-1}\text{Mpc}$ to define the cosmic web. After varying the numerical parameters in our experiments we find that the halo shape presents the strongest alignment along the smallest tidal eigenvector, i.e. along filaments and walls, with a signal that gets stronger as the halo mass increases. In the case of the velocity shear field only massive halos $> 10^{12}h^{-1}M_{\odot}$ tend to have their shapes aligned along the largest tidal eigenvector; that is perpendicular to filaments and walls. For the angular momentum we find alignment signals only for halos more massive than $10^{12}h^{-1}M_{\odot}$ both in the tidal and velocity shear webs where the preferences are for it to be parallel to the middle eigenvector; perpendicular to filaments and parallel to walls. Finally, the peculiar velocities show a strong alignment along the smallest tidal eigenvector for all halo masses; moving along filaments and walls. In the velocity shear the same alignment is present but weaker and only for halos less massive than $10^{12}h^{-1}M_{\odot}$. Most of the different signals between the two web descriptions are due to the fact that the main directions of stronger tidal tension and velocity shear coincide for halos below $10^{12}h^{-1}M_{\odot}$ but are perpendicular to each other for halos more massive than this threshold. Our results clearly show that the two different algorithms we used to define the cosmic web describe different physical aspects of non-linear collapse and should be used in a complementary way to understand the effect of the cosmic web on galaxy evolution.

Key words: methods: numerical, galaxies: haloes, cosmology: theory, dark matter, large-scale structure of Universe

1 INTRODUCTION

There is a long observational tradition studying galactic properties as a function of their large scale environment (e.g. Oemler 1974; Dressler 1980; Pimbblet et al. 2002; Gómez et al. 2003; Kauffmann et al. 2004; Abbas & Sheth 2006; Baldry et al. 2006; Park et al. 2007; O’Mill et al. 2008; González & Padilla 2009; Padilla et al. 2010; Wilman et al. 2010; Muldrew et al. 2012). In these situations the environment definition is usually based on quantities easily accessible to observations such as local number density or nearest neighbour measurements. With the advent of large surveys

the visibility of the cosmic web became clear. As a consequence, in order to capture its filamentarity, the environment definition started to be more complex, involving shear and gradient properties of the galaxy density field or the reconstructed dark matter density/velocity field (Lee et al. 2005; Aragón-Calvo et al. 2007; Hahn et al. 2007; Sousbie et al. 2008; Zhang et al. 2009; Muñoz-Cuartas et al. 2011; Hoffman et al. 2012; Trowland et al. 2013; Tempel et al. 2014, e.g.).

In parallel to the observational advances, numerical simulations successfully reproduced the web-like structure of the galaxy distribution in models based on gravitational in-

stability in a Dark Matter (DM) dominated universe (e.g. Bond et al. 1996; Colberg et al. 2005). Simulations now allow to follow the time evolution into the deep non-linear regime of virialized structures (DM halos) which in turn should host observable galaxies to study their evolution in the cosmic web. The discovery in simulations of gas filaments that feed galaxies is another theoretical hint that strengthened the expected connection between galactic properties and their place in the web (Ocvirk et al. 2008; Dekel et al. 2009).

In the last decade new algorithms have implemented cosmic web classifications that go beyond the local density by defining a location to be a peak, sheet, filament or void depending on the symmetry properties of the local dark matter distribution. With the aid of simulations it has been established that halos of a given mass form earlier in denser regions; concentration, angular momentum and shape can also be aligned with these web elements. (e.g. Aragón-Calvo et al. 2007; Hahn et al. 2007; Forero-Romero et al. 2009; Zhang et al. 2009; González & Padilla 2010; Noh & Cohn 2011; Codis et al. 2012; Libeskind et al. 2013; Trowland et al. 2013).

The observational studies that try to measure angular momentum correlations use the galaxy shape as a proxy (Lee & Pen 2002; Lee & Erdogdu 2007; Jones et al. 2010; Paz et al. 2008). In this respect it is useful to have a theoretical baseline for the correlations of angular momentum and shape with the cosmic web. There is large tradition of alignment measurements of shape and angular momentum (e.g. Hahn et al. 2007; Aragón-Calvo et al. 2007; Zhang et al. 2009; Paz et al. 2011; Codis et al. 2012; Trowland et al. 2013; Libeskind et al. 2013; Aragón-Calvo & Yang 2014). The main result of these previous studies is that shape alignment is a robust measurement regardless of the methods and simulations. On the other hand, the results for the angular momentum differ in the degree of the alignment.

In the same spirit of describing the place of galaxies within the cosmic web, there has been a revival of surveys that measure the cosmic flow patterns in the Local Universe (Nusser et al. 2011; Tully et al. 2013). Assuming the linearity between the divergence of the cosmic flow velocity field and the local matter overdensity (valid in the linear regime) one could construct accurate maps of the matter density from peculiar velocities (Courtois et al. 2012). From this perspective it is interesting to look at the expected alignment of the peculiar velocities.

In this paper we review most of the studies about shape and angular momentum alignment and offer our own study with complementary numerical techniques and simulations. We also present for the first time in the literature new results for the alignment of peculiar velocities with the large scale structure.

The structure of this paper is the following. In §2 we present the theoretical antecedents for the alignment studies we present in this paper. In §3 we present the N-body cosmological simulation and halo catalogs. Next, we describe in §4 the two web-finding algorithms we use and in §5 the setup for our numerical experiments. In §6 we present our main results about the alignment of shape, angular momentum and peculiar velocities with respect to the cosmic web. In §7 we present our conclusions.

2 THEORETICAL CONSIDERATIONS: NOTATION AND PRECEDENTS

Out of the three alignments that we study in this paper - shape, angular momentum and peculiar velocity- only the first two have received wide attention in the literature, being angular momentum the most popular with twice the number of studies for shape alignment.

In this paper we focus our attention on results published during the last decade that have made use of large N-body dark matter only cosmological simulations. There are many works that have addressed this problem using observational data from large surveys such as the Sloan Digital Sky Survey (SDSS), however we choose to narrow our discussion to simulation based studies which are directly comparable to the one we present here.

Alignments are often measured from the distribution of the $\mu = |\cos \theta|$ where θ is the angle between the two axes of interest. This is often directly measured as the absolute value of the dot product between the two unit vectors along the directions being tested. For instance, in the case of angular momentum one would compute $\mu = |\hat{j} \cdot \hat{n}|$. In the case of shape alignments the major axis is the chosen direction to compare against the cosmic web.

For an isotropic distribution of the vector around the direction defined by \hat{n} the μ distribution, ranging between 0 and 1, should be flat and its mean value should be $\langle \mu \rangle = 0.5$. If a distribution is biased towards 1 ($\langle \mu \rangle > 0.5$) we call this an statistical alignment along \hat{n} , while in the case of a bias towards 0 ($\langle \mu \rangle < 0.5$) we talk about an anti-alignment, meaning a perpendicular orientation with respect to the \hat{n} direction.

Trowland et al. (2013) presented a parameterization for the μ distribution in the case of angular momentum alignment based on theoretical considerations by Lee et al. (2005) (Eq. 6 in the Appendix A). Under this parameterization a unique correspondence was found between the full shape of the $|\mu|$ distribution and its average. In this paper we follow the lines of their work but only present the results for the average $\langle |\mu| \rangle$.

Table 1 and Table 2 summarize recent results found in the literature for shape and angular momentum alignment. The Appendix A includes a detailed description of the definitions, algorithms and simulations used in each one of these studies. In these tables the first column describes the reference, the second column summarizes the web finding method with a single name, the third associates a spatial scale to the web finding methods, in most cases it corresponds to the grid size or smoothing scale used to interpolate the underlying matter density or velocity field; The fourth column indicates along which web element (filament or wall) the alignment was measured; the fifth column indicates the strength of the alignment/anti-alignment, ++/-- indicate a strong alignment/anti-alignment while +/- indicate a weaker signal; the last column indicates whether the described signal is present within a defined range of halo mass.

These results can be summarized in three important points:

- The halo mass of $1 - 5 \times 10^{12} h^{-1} M_{\odot}$ is a threshold mass between behaviours of no-alignment, alignment or anti-alignment.

- Halo shape provides a strong alignment signal along filaments and sheets, more so for massive haloes.
- Halo spin tends to be oriented perpendicular to filaments and parallel to sheets, but it is a weaker than shape alignment.

A novel aspect of our study is the use of a single computational volume of a high resolution simulation to study the alignments. Equally important, is our focus to quantify to what extent these results depend on the method used to define the cosmic web and the numerical choices to implement the algorithms.

3 N-BODY SIMULATION AND HALO CATALOGUE

In this paper we use the Bolshoi simulation that follows the non-linear evolution of a dark matter density field on cosmological scales. The volume is a cubic box with $250h^{-1}\text{Mpc}$ on a side, the matter density field is sampled with 2048^3 particles. The cosmological parameters in the simulation correspond to the results inferred from WMAP5 data (Dunkley et al. 2009), which are also consistent with the more recent results of WMAP9 (Hinshaw et al. 2013). These parameters are $\Omega_m = 0.27$, $\Omega_\Lambda = 0.73$, $\sigma_8 = 0.82$, $n_s = 0.95$ and $h = 0.70$ for the matter density, cosmological constant, normalization of the power spectrum, the slope in the spectrum of the primordial matter fluctuation and the dimensionless Hubble constant. With these conditions the mass of each dark matter particle in the simulation corresponds to $m_p = 1.4 \times 10^8 h^{-1} \text{M}_\odot$. A more detailed description of the simulation can be found in (Klypin et al. 2011).

In this paper we use groups identified with a Friends-Of-Friends (FOF) halo finder using a linking length of $b = 0.17$ times the mean interparticle separation. This choice translates into halos with a density of 570 times the mean density at $z = 0$. The measurements for the shape, angular momentum and peculiar velocity are done using the set of particles in each dark matter halo. The definition we use in this paper for the shape comes from the diagonalization of the reduced inertia tensor.

$$\tau_{lm} = \sum_i \frac{x_{i,l} x_{i,m}}{R_i^2}, \quad (1)$$

where i is the particle index in the halo and l, m run over the three spatial indexes and $R_i^2 = x_{i,1}^2 + x_{i,2}^2 + x_{i,3}^2$, where the positions are measured with respect to the center of mass.

The angular momentum is calculated as

$$\vec{J} = \sum_i m_p R_i \vec{v}_i, \quad (2)$$

where the velocities are also measured with respect to the center of mass velocity. Finally the peculiar velocity of a halo is computed as the center of mass velocity.

The halo and environment used in this paper is publicly available through the MultiDark database¹. The halo data is thoroughly described in Riebe et al. (2013).

4 WEB FINDING ALGORITHMS

We use two algorithms to define the cosmic web in cosmological N-body simulations. Both are based on the same algorithmic principle, which determines locally a symmetric tensor which can be diagonalized to yield three real eigenvalues $\lambda_1 > \lambda_2 > \lambda_3$ and their corresponding eigenvectors \mathbf{e}_1 , \mathbf{e}_2 and \mathbf{e}_3 . This allows for a local classification into one of the following four web types: void, sheet, filament and peak depending on whether the number of eigenvalues larger than a given threshold λ_{th} is 3, 2, 1 or 0, respectively.

We use two different symmetric tensors. The first is the shear tensor, defined as the Hessian of the gravitational potential, normalized in such a way as to be dimensionless:

$$T_{\alpha\beta} = \frac{\partial^2 \phi}{\partial r_\alpha \partial r_\beta}, \quad (3)$$

where ϕ is the gravitational potential rescaled by a factor $4\pi G \bar{\rho} = 3/2 \Omega_m H_0^2$ in such a way that the Poisson equation can be written as $\nabla^2 \phi = \delta$, where δ is the matter overdensity, $\bar{\rho}$ is the average matter density, H_0 is the Hubble constant at the present time and Ω_m is the matter density parameter. A detailed presentation of this algorithm can be found in Forero-Romero et al. (2009).

The second tensor is the velocity shear:

$$\Sigma_{\alpha\beta} = -\frac{1}{2H_0} \left(\frac{\partial v_\alpha}{\partial r_\beta} + \frac{\partial v_\beta}{\partial r_\alpha} \right), \quad (4)$$

where the v_α correspond to the components of the peculiar comoving velocities. With this definition the trace of the shear tensor is minus the divergence of the velocity field normalized by the Hubble constant $-\nabla \cdot \mathbf{v}/H_0$. A detailed description of this algorithm can be found in Hoffman et al. (2012).

4.1 Numerical considerations

In this paper we compute the cosmic web on cubic grids of two different resolutions 256^3 and 512^3 that roughly correspond to scales of 1 and $0.5h^{-1}\text{Mpc}$, respectively. For the T-Web we interpolate first the matter density field using a Cloud-In-Cell (CIC) scheme. Then we smooth using a Gaussian kernel with a spatial variance equal to the size of one grid cell. This smoothed matter density field is transformed into Fourier space to solve the Poisson equation and find the gravitational potential ϕ . The Hessian is computed using a finite differences method. Finally, the eigenvalues and eigenvectors are computed on each grid point.

For the V-Web we interpolate first the momentum density field over a grid using the CIC scheme and then apply a gaussian smoothing with a spatial variance of one grid cell. We use the matter density field, which is also CIC interpolated and gaussian smoothed, to normalize the momentum field. This ratio between the momentum and matter density field is what we consider as the velocity field to compute the shear tensor on each grid point. In this case we also compute the eigenvalues and eigenvectors on each grid point.

We caution the reader that the results reported by (Hoffman et al. 2012; Libeskind et al. 2013; Wang et al. 2013) use a velocity field that is calculated by a gaussian

¹ <http://www.multidark.org/MultiDark/>

Author	Web Method	Spatial Scale	Along	Alignment	Mass dependence
Forero-Romero et al. (2014)	T-Web	$0.5 - 1h^{-1}\text{Mpc}$	\hat{e}_3 (filament)	++	$> 10^{12}h^{-1}\text{M}_\odot$
			\hat{e}_3 (filament)	+	$< 10^{12}h^{-1}\text{M}_\odot$
			\hat{e}_1 (wall)	++	$> 10^{12}h^{-1}\text{M}_\odot$
			\hat{e}_1 (wall)	+	$< 10^{12}h^{-1}\text{M}_\odot$
Forero-Romero et al. (2014)	Vp-Web	$0.5 - 1h^{-1}\text{Mpc}$	\hat{e}_3 (filament)	--	$> 10^{12}h^{-1}\text{M}_\odot$
			\hat{e}_3 (filament)	none	$< 10^{12}h^{-1}\text{M}_\odot$
			\hat{e}_1 (wall)	--	$> 10^{12}h^{-1}\text{M}_\odot$
			\hat{e}_1 (wall)	none	$< 10^{12}h^{-1}\text{M}_\odot$
Libeskind et al. (2013)	V-Web	$1h^{-1}\text{Mpc}$	filament	++	$> 10^{12}h^{-1}\text{M}_\odot$
			filament	+	$< 10^{12}h^{-1}\text{M}_\odot$
			wall	++	all masses
Zhang et al. (2009)	Hessian density field	$2.1h^{-1}\text{Mpc}$	filament	++	$> 10^{12}h^{-1}\text{M}_\odot$
			filament	+	$< 10^{12}h^{-1}\text{M}_\odot$
Aragón-Calvo et al. (2007)	Hessian density field	-	wall	++	$> 10^{12}h^{-1}\text{M}_\odot$
		-	wall	+	$< 10^{12}h^{-1}\text{M}_\odot$
		-	filament	++	$> 10^{12}h^{-1}\text{M}_\odot$
		-	filament	+	$< 10^{12}h^{-1}\text{M}_\odot$

Table 1. Shape alignment with the cosmic web. Summary of theoretical results provided by methods similar to ours.

Author	Web Method	Spatial Scale ($h^{-1}\text{Mpc}$)	Along	Alignment	Mass dependence
Forero-Romero et al. (2014)	T-Web	$0.5 - 1$	\hat{e}_3 (filament)	-	$> 10^{12}h^{-1}\text{M}_\odot$
			\hat{e}_3 (filament)	none	$< 10^{12}h^{-1}\text{M}_\odot$
			\hat{e}_1 (wall)	none	$> 10^{12}h^{-1}\text{M}_\odot$
			\hat{e}_1 (wall)	none	$< 10^{12}h^{-1}\text{M}_\odot$
Forero-Romero et al. (2014)	Vp-Web	$0.5 - 1$	\hat{e}_3 (filament)	none	$> 10^{12}h^{-1}\text{M}_\odot$
			\hat{e}_3 (filament)	none	$< 10^{12}h^{-1}\text{M}_\odot$
			\hat{e}_1 (wall)	+	$> 10^{12}h^{-1}\text{M}_\odot$
			\hat{e}_1 (wall)	none	$< 10^{12}h^{-1}\text{M}_\odot$
Libeskind et al. (2013)	V-Web	1	filament	-	$> 10^{12}h^{-1}\text{M}_\odot$
			filament	+	$< 10^{12}h^{-1}\text{M}_\odot$
			wall	++	all masses
Trowland et al. (2013)	Hessian density	$2 - 5$	filament	-	$> 5 \times 10^{12}h^{-1}\text{M}_\odot$
			filament	+	$< 5 \times 10^{12}h^{-1}\text{M}_\odot$
Codis et al. (2012)	Morse Theory & T-Web	$1 - 5$	filament	--	$> 10^{12.5}h^{-1}\text{M}_\odot$
			filament	++	$< 10^{12.5}h^{-1}\text{M}_\odot$
			wall	++	all masses
Zhang et al. (2009)	Hessian density	2.1	filament	++	if anticorrelated with shape
			filament	--	if correlated with shape
Aragón-Calvo et al. (2007)	Hessian density	-	wall	++	$> 10^{12}h^{-1}\text{M}_\odot$
		-	wall	+	$< 10^{12}h^{-1}\text{M}_\odot$
		-	filament	-	$> 10^{12}h^{-1}\text{M}_\odot$
		-	filament	+	$< 10^{12}h^{-1}\text{M}_\odot$
Hahn et al. (2007)	Tidal Web	2.1	filament	-	none
			wall	++	$> 10^{12}h^{-1}\text{M}_\odot$
			wall	+	$< 10^{12}h^{-1}\text{M}_\odot$

Table 2. Angular momentum alignment with the cosmic web. Summary of theoretical results provided by methods similar to ours.

smoothing of the CIC velocity field without taking into account any weight by mass.

5 OUR NUMERICAL EXPERIMENTS

In this paper we use the data and the methods described above to perform two kinds of measurements: the preferential alignment and the average value of the angle along the eigenvectors of interest.

We note that we measure alignments along the eigenvectors of the cosmic web without defining first whether each point corresponds to a filament or a wall. However, for simplicity and readability we describe our results in terms of alignment with respect to filaments and sheets. Given that the direction along a filament should be defined by the eigenvector \hat{e}_3 corresponding to the smallest eigenvalue λ_3 , a strong alignment along that vector will be reported as an alignment along filaments. Correspondingly, the first eigenvector \hat{e}_1 defines the direction perpendicular to walls, a strong alignment along this vector will be reported as an anti-alignment along walls. Finally, a strong alignment along the second eigenvector \hat{e}_2 in company with an anti-alignment with \hat{e}_1 is reported as an alignment with walls and anti-alignment with respect to filaments.

We avoid the classification into filaments and walls for the following reason. Partitioning the simulation into web elements implies a choice regarding the value for the parameter λ_{th} in two different web finders. This has been done before for each web finder independently. However, we consider that deriving results independent of the choice of parameters $\lambda_{\text{th,TWEB}}$, $\lambda_{\text{th,VWEB}}$ provides clear data to understand the connection of DM halos with the cosmic web.

However, a possible disadvantage is that we are mixing the alignment signal of different environments. For instance, if half of the halo population of fixed mass is aligned along filaments (the vector \hat{e}_3), and the other half along planes (perpendicular to \hat{e}_1 but without a clear signal along \hat{e}_3 , \hat{e}_2), the total signal of the alignment along \hat{e}_3 might appear diluted in comparison to a signal taken separately for filaments and walls. However, as it has been shown in Libeskind et al. (2013) the alignment signals are robust across different environments.

5.1 Preferential Alignment

The first measurement is a rough approximation to find out along which axes halos are aligned. We refer to this as Preferential Alignment (PA).

We use the fact that for a given vector under study \hat{s} and the three eigenvectors the following identity holds

$$(\hat{s} \cdot \hat{e}_1)^2 + (\hat{s} \cdot \hat{e}_2)^2 + (\hat{s} \cdot \hat{e}_3)^2 = 1. \quad (5)$$

Using this we know that all halos can be splitted into three groups:

- (i) Halos with $(\hat{s} \cdot \hat{e}_1)^2 > (\hat{s} \cdot \hat{e}_2)^2$ and $(\hat{s} \cdot \hat{e}_1)^2 > (\hat{s} \cdot \hat{e}_3)^2$, which can be considered to aligned mostly along \hat{e}_1 .
- (ii) Halos with $(\hat{s} \cdot \hat{e}_2)^2 > (\hat{s} \cdot \hat{e}_1)^2$ and $(\hat{s} \cdot \hat{e}_2)^2 > (\hat{s} \cdot \hat{e}_3)^2$, which can be considered to aligned mostly along \hat{e}_2 .

- (iii) Halos with $(\hat{s} \cdot \hat{e}_3)^2 > (\hat{s} \cdot \hat{e}_1)^2$ and $(\hat{s} \cdot \hat{e}_3)^2 > (\hat{s} \cdot \hat{e}_2)^2$, which can be considered to aligned mostly along \hat{e}_3 .

If the halo population does not show any preferential alignment, then all the halos must be evenly distributed along these three populations. On the contrary, if there is more than one third of the halo population in one of these sets, then this will indicate a preferential alignment along one of the axes. However, this statistics does not give a precise answer on the degree of the alignment

5.2 Average Alignment Angle

We emphasize that we focus on the alignments with respect to the eigenvectors regardless of the web type. We recall that the eigenvector \hat{e}_1 is perpendicular to the plane defining a sheet and the line describing a filament; and \hat{e}_3 is the vector that marks the direction of a filament and lies on the plane of a sheet. Therefore we focus on quantifying the degree of alignment along these two eigenvectors.

This experiment complements the results obtained by the PA statistic by computing the average and standard deviation of $|\langle \hat{s} \cdot \hat{e}_1 \rangle|$ and $|\langle \hat{s} \cdot \hat{e}_3 \rangle|$. We perform these tests in different populations split into different mass bins logarithmically spaced between $1 \times 10^9 h^{-1} \text{M}_\odot$ and $1 \times 10^{14} h^{-1} \text{M}_\odot$.

In a separate test we make the same measurements but this time splitting the halo sample by other properties such as: circularity, concentration, local matter density, spin and triaxiality. In this case we take the upper and lower 30% of the halos according to each property and measure the strength of the alignment by the average value of $|\langle \hat{s} \cdot \hat{e}_1 \rangle|$ and $|\langle \hat{s} \cdot \hat{e}_3 \rangle|$.

6 RESULTS

6.1 Preferential Alignment

Figure 1 presents all the results for the preferential alignment (PA) summarizing to a good extent the main results of this paper.

The shape alignment and the Vweb (upper row, left column) gives a different perspective. Firstly, there seems to be little evidence for an alignment for masses below $10^{11} - 10^{12} h^{-1} \text{M}_\odot$, depending on the grid resolution. Secondly, the alignment at higher masses goes along the first eigenvector \hat{e}_1 meaning that they mostly lie perpendicular to the filaments and sheets. In the discussion section we clarify this result that at first sight might seem puzzling.

For shape alignment and the Tweb (upper row, right column) we find a strong preferential alignment along the third eigenvector \hat{e}_3 . This signal increases steadily with mass and is almost independent of the grid resolution. At high masses between 70% and 100% of the halos have their major axis aligned along \hat{e}_3 which means that they mostly lie along filaments and sheets.

The angular momentum in the Vweb (middle row, left column) presents a signal of alignment along the second eigenvector \hat{e}_2 ; between 45% to 60% of the halos are aligned along that direction, while there is a minority of halos aligned with \hat{e}_1 . There is a clear change in trends around $10^{11} h^{-1} \text{M}_\odot - 10^{12} h^{-1} \text{M}_\odot$ depending on the grid resolution; below that mass range there is no evidence for alignment



Figure 1. Fraction of halos in a mass bin that show a preferential alignment with respect to an eigenvector in the cosmic web; \hat{e}_1 (black) defines the direction perpendicular to a wall and \hat{e}_3 (yellow) indicates the direction along a filament. Each row presents one of the three properties studied in this paper: shape (major axis), angular momentum and peculiar velocity. The left (right) column presents the results against the Vweb (Tweb). Strong colors refer to 256^3 grid resolutions and lighter colors to a 512^3 grid. The thick black horizontal line at 0.33 corresponds to the expected fraction for a random vector field. The uncertainty is computed assuming poissonian statistics in each mass bin.

while at higher masses all the trends we describe are noticeable. This means that the angular momentum of halos above $10^{12} h^{-1} M_\odot$ tends to lie along walls, parallel to the vector \vec{e}_2 ; without any clear trend for alignment/anti-alignment with respect to filaments.

For the angular momentum alignment and the Tweb (middle row, right column) we find no evidence for any alignment at low masses $< 10^{12} h^{-1} M_\odot$. At higher masses $> 10^{12} h^{-1} M_\odot$ there is a weak signal of preferential alignment along the first and second eigenvectors; between 35% to 45% of the halos are aligned with respect to \vec{e}_1 and \vec{e}_2 . Correspondingly, between 10% to 20% of the halos are aligned

along \vec{e}_3 . This means that most of the halos are perpendicular to the filaments and do not have a clear alignment with respect to walls.

The peculiar velocities (lower panels) show a weak but consistent alignment along the third eigenvector \vec{e}_3 of the Tweb for all masses below $10^{13.0} h^{-1} M_\odot - 10^{13.5} h^{-1} M_\odot$ depending on the grid resolution. 45% of the halos are aligned this way, while only 25% are aligned along the first eigenvector \vec{e}_1 . This suggests that halos tend to move along filaments and parallel to the walls, except at higher masses where the alignments get randomized. In contrast, the pe-

cular velocities with respect to the Vweb show the same, although weaker, trend and only for low mass halos $< 10^{12}$.

In the next subsections we present a complementary account of these results by showing quantitative results of the average angle between vector pairs describing the alignments discussed so far.

6.2 Shape Alignment

Figure 2 presents the main results for the angles between the first and third eigenvectors and the major shape axis as a function of halo mass. Notice that the errorbars shown correspond to the 20 and 80 percentiles; the actual error of the medians are always small, $\sim 1-5$ percent, and therefore are not shown.

In the case of the Vweb (left column) we have a clear alignment with respect to the first eigenvector at high masses $> 10^{12}h^{-1}M_{\odot}$, with values $|\langle \cos \theta \rangle| \approx 0.8$ well above the expected value of 0.5 for a random distribution. With respect to the third eigenvector we measure an anti-alignment with $|\langle \cos \theta \rangle| \approx 0.3$. For low masses $< 10^{12}h^{-1}M_{\odot}$ we do not detect any alignment signal. This is consistent with the PA results of massive halos perpendicular to filaments and parallel to walls.

The Tweb (right column) shows alignment trends starting at masses of $10^{10}h^{-1}M_{\odot}$, two orders of magnitude below than the Vweb. In this case we measure an alignment along the third eigenvector and an anti-alignment along the first eigenvector. In the latter case at the highest masses $|\langle \cos \theta \rangle| \approx 0.8$, while in the former at $|\langle \cos \theta \rangle| \approx 0.2$. This strong alignment/anti-alignment signal mirrors the interpretation from the PA results that describe halos lying parallel both to filaments and walls.

6.3 Angular Momentum Alignment

We now focus our attention on the angular momentum alignment. Figure 3 shows the results as a function of halo mass following the same panel layout as in Figure 2. In all cases we see that these alignment trends are weaker than the shape alignments. For the Vweb low mass halos $< 10^{12}h^{-1}M_{\odot}$ do not show any preferential alignment with the cosmic web. Halos more massive than this threshold have their angular momentum slightly perpendicular to the direction defined by the first eigenvector and are uncorrelated with the third eigenvector. This translates into a weak tendency for the angular momentum to lie parallel to walls.

In the case of the Tweb, the alignment for low mass halos $< 10^{12}h^{-1}M_{\odot}$ is also absent. More massive halos present a weak alignment along first eigenvector and anti-alignment with the third eigenvector. This provides a quantitative expression of the results derived from the preferential alignment whereby the angular momentum is weakly perpendicular to filaments.

6.4 Peculiar Velocity Alignment

Figure 4 shows the results for peculiar velocities alignments. In the case of the Vweb, the peculiar velocities show a weak signal of alignment ($|\langle \cos \theta \rangle| \approx 0.55$) along the third eigenvector for low masses $< 10^{12}M_{\odot}$ and a weak anti-alignment

at higher masses. The strength of the alignment also shows a clear dependency on the grid size used to compute the web.

The Tweb shows a stronger alignment with the third eigenvector at all masses with $|\langle \cos \theta \rangle| \approx 0.6$ and an anti-alignment with the first eigenvector with $|\langle \cos \theta \rangle| \approx 0.4$. In contrast to the Vweb results, these trends remain basically unchanged at all masses and grid resolutions, with only minor changes for halos masses $> 10^{13}h^{-1}M_{\odot}$.

6.5 What drives the alignment

We wish to understand what other selection criteria on halo properties can produce a stronger local alignment for the shape, spin and peculiar velocities. We split the halo population into low and high mass halos imposing a cut at $M_{\text{halo}} = 10^{11}h^{-1}M_{\odot}$. This allows us to have robust statistics on the high mass end. We have also computed these results for a cut at $M_{\text{halo}} = 10^{12}h^{-1}M_{\odot}$ and checked that the results we report below are not affected by this change.

For each mass interval we perform cuts in the following properties: halo spin, concentration, halo triaxiality defined as $(a^2 - b^2)/(a^2 - c^2)$ with high (low) triaxiality corresponding to prolate (oblate) shapes, circularity (c/a) and halo inner density (virial mass divided by volume out to the virial radius). We measure the web alignments in two sets, each one including the 30% of halos in the lower/higher end of the corresponding property.

Figure 5 shows the results for the major axes of the Vweb and Tweb (left and right panels) and the shape major axis, the angular momentum vector, and the halo peculiar velocity (top, middle and bottom panels, respectively). As here we show the average of the halo population above the lower mass limit imposed, the halo masses that dominate the statistics are close to this lower limit $10^{11}h^{-1}M_{\odot}$. We show the result for the Tweb and Vweb calculated using the two available resolutions, but as can be seen in general we find no significant differences in our results.

Halos with higher circularity and inner density show a higher alignment with the Vweb major axes. The opposite is the case of haloes with higher concentration, spin and triaxiality. This trend is also visible in the angular momentum vs. Vweb major axis alignment only for the concentration and spin, with little differences evidenced by the other halo properties. The alignment strengthening is somewhat reversed when comparing the Vweb with the halo peculiar velocity, with some evidence for a strengthening with lower circularity and inner density, and a weakening with spin and triaxiality.

On the right panels the trends can also be readily seen. The Tweb vs. major axis alignments are stronger for higher circularity, concentration and inner density, and weaker for higher spins and triaxialities. With respect to the angular momentum, the alignment is weaker for higher circularities, concentrations, inner densities and spins, and is only strengthened when the triaxiality is higher. Not much difference is seen in the Tweb vs. halo peculiar velocity alignments, being this the only regime where there is a clear difference in influence of halo properties on the alignments with the Tweb and Vweb; the latter do show important changes on the lower-left panel.

As can be seen, higher concentrations, circularities and densities, as well as lower spins and triaxialities, produce a

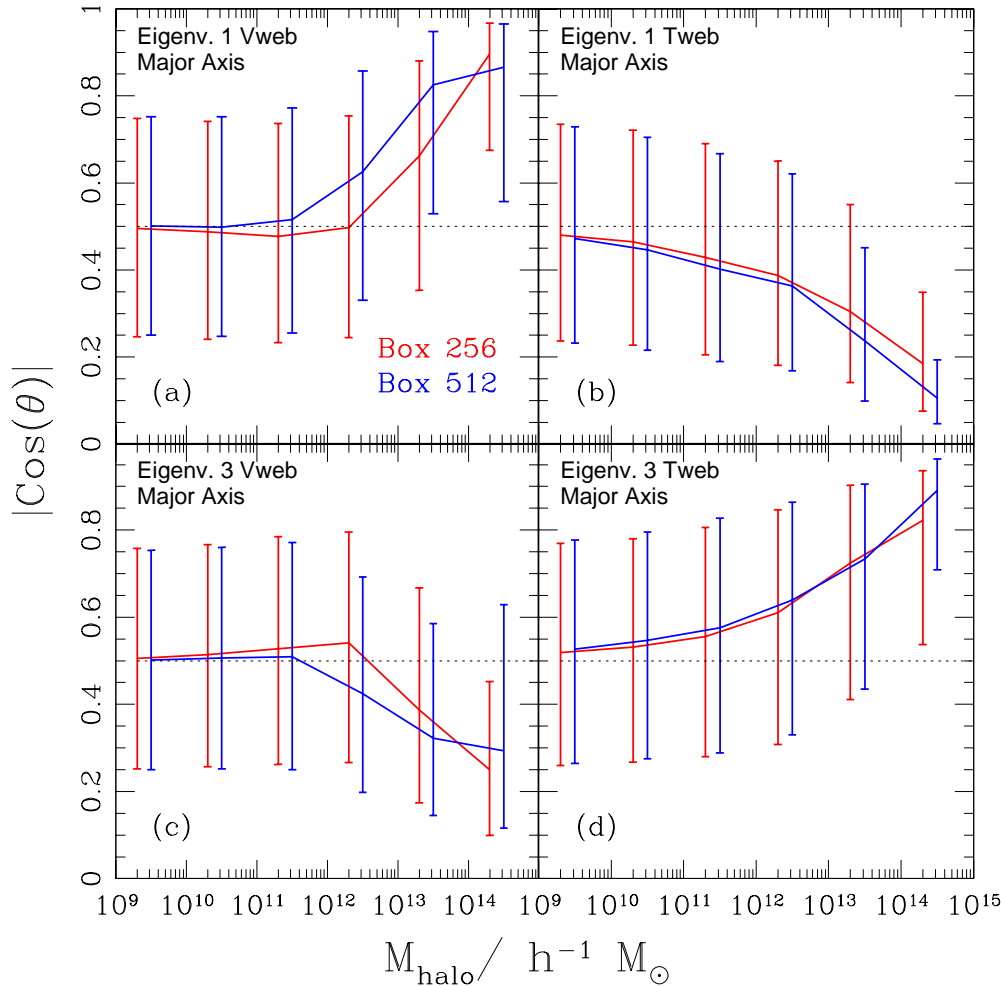


Figure 2. Median of $|\cos\theta|$ quantifying the shape alignment for the Vweb (left) and the Tweb (right) at two different grid resolutions as a function of halo mass. The errorbars show the 20 and 80 percentiles of the distribution; the errors on the median are too small to be noticed in this figure. In the upper (lower) panels the angle θ is measured between the halo major axis and the first (third) eigenvector.

similar effect on the Tweb vs. major axis alignments to that of diminishing the mass of the halos. This has also been detected in other halo properties such as their clustering amplitude in what has been termed assembly bias (e.g. Gao et al. 2005; Li et al. 2008; Lacerna & Padilla 2011) where halos of different ages and equal mass show different clustering amplitudes, which could also be interpreted as a change in the effective halo mass according to halo properties.

An older halo age has been shown to come along with more spherical halo shapes, higher concentrations and halo inner density. However, in the assembly bias scenario of Gao et al. (2005), these halos tend to show a clustering amplitude consistent with that of the median halo population of higher masses. In terms of the alignments with the Tweb, our results show the opposite trend. This shows that the physics behind the clustering amplitude and alignments do not necessarily coincide. The full understanding of the dependence of halo properties and/or on their environment is a complex problem, but these results provide extra information that complements that obtained from clustering measurements.

6.6 Interweb Alignment

Perhaps the most striking result so far is that the two webs algorithms gives different results for the alignment of massive halos. This is not completely unexpected given that the two algorithms are based on different physical premises to obtain the directions defining the eigenvectors. However, we investigate the origin of the different alignment statistics by studying the inter-web alignment.

For the two algorithms, Tweb and Vweb, we have the information for their eigenvectors and eigenvalues on exactly the same positions defined by the grids. This allows us to compute the pair-wise alignment between the eigenvectors in the two web finders.

We restrict our analysis to the grid cells that are occupied by halos. Otherwise, if we decided to perform this kind of analysis on all the grid cells, the statistics would be more representative of the void regions as they dominate in number the fraction of cells in the simulation.

Figure 6 shows the values for $|\langle\cos\theta\rangle|$ between the two \vec{e}_1 eigenvectors in the Tweb and the Vweb. The Figure shows

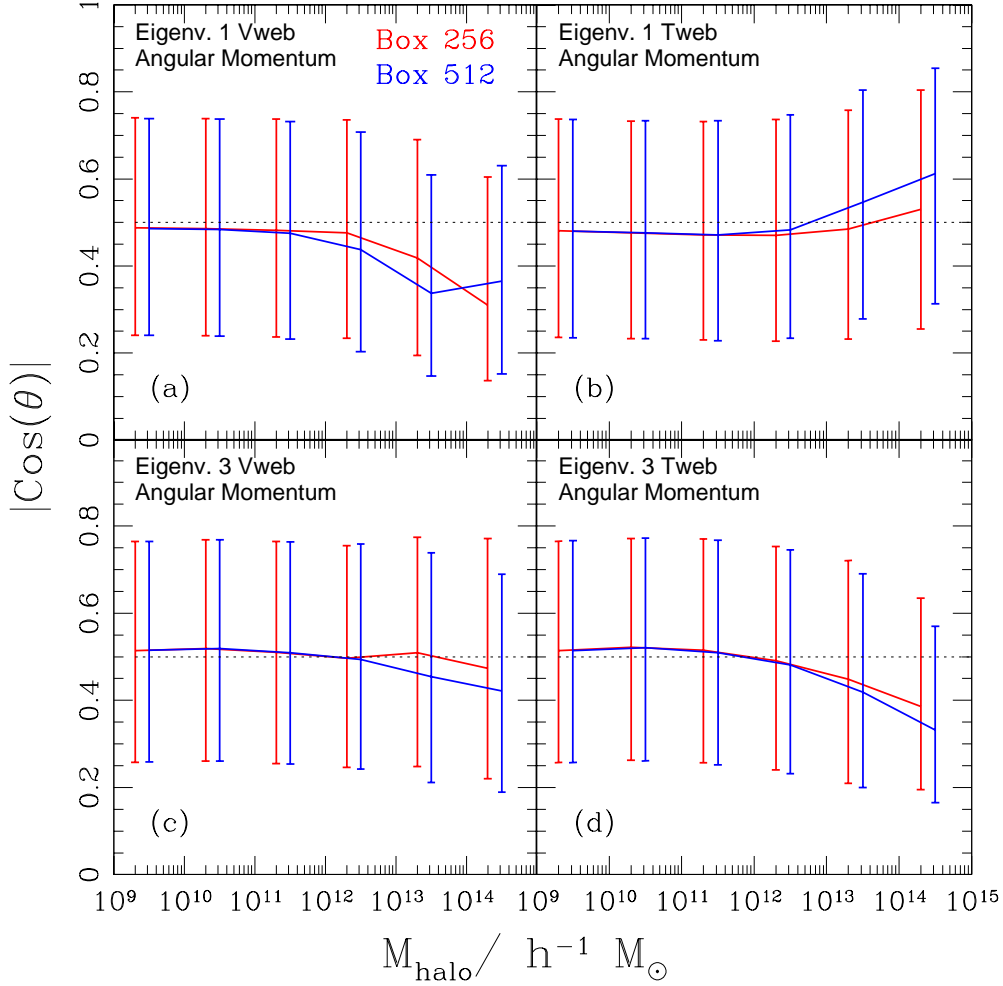


Figure 3. Median of $|\cos\theta|$ quantifying the angular momentum alignment for the Vweb (left) and the Tweb (right) for two different grid resolutions as a function of halo mass. In the upper (lower) panels the angle θ is measured between the first (third) eigenvector and the angular momentum vector.

that there is an alignment, $|\langle\cos\theta\rangle| \approx 1.0$, for low mass halos and an anti-alignment, $|\langle\cos\theta\rangle| \approx 0.2$ for massive ones.

The transitional scale is located around $(10^{11.5} - 10^{12.5})h^{-1}\text{M}_\odot$ depending on the grid resolution. The coarse grid (256^3) shows the transition at higher masses than the fine grid (512^3). We also note that the alignment is weaker in the finer grid, ($|\langle\cos\theta\rangle| \approx 0.7$) than in the coarser grid ($|\langle\cos\theta\rangle| \approx 1.0$).

These two facts (alignment at low masses and low grid resolution) points towards an explanation in terms of the linear / non-linear growth of structure. When the alignment is present on linear scales the divergence of the velocity field is proportional to the overdensity, i.e. the trace of the shear field is proportional to the trace of the tidal field.

On the scale where the halos more massive than $10^{13}h^{-1}\text{M}_\odot$ are located, the relationship between the velocity shear and the tidal field changes. There, the fastest momentum-weighted collapse direction (defined by the Vweb) is perpendicular to the direction where the tidal compression is the highest.

It is possible to consider that numerical effects can also affect the estimation of the eigenvectors. For instance, dif-

ferent levels of shot noise in the interpolation scheme to construct the density and momentum grids could contribute to the anti-alignment of the two algorithms. However, a detailed study of the inter-web alignments is beyond the scope of this paper.

7 CONCLUSIONS

We have examined the alignment of shape, angular momentum and peculiar velocity of dark matter halos with respect to the cosmic web. We use publicly available data from two algorithms implemented on a large cosmological N-body simulation to study halo populations spanning five orders of magnitude in mass. The first algorithm uses the tidal field (Tweb) and the second the velocity shear (Vweb); both include results on spatial scales of $0.5h^{-1}\text{Mpc}$ and $1.0h^{-1}\text{Mpc}$.

We quantify the alignments in two complementary ways. The first one measures the fraction of halos in a population that is preferentially aligned with either one of the eigenvectors \vec{e}_1 , \vec{e}_2 or \vec{e}_3 in the local definition of the cosmic

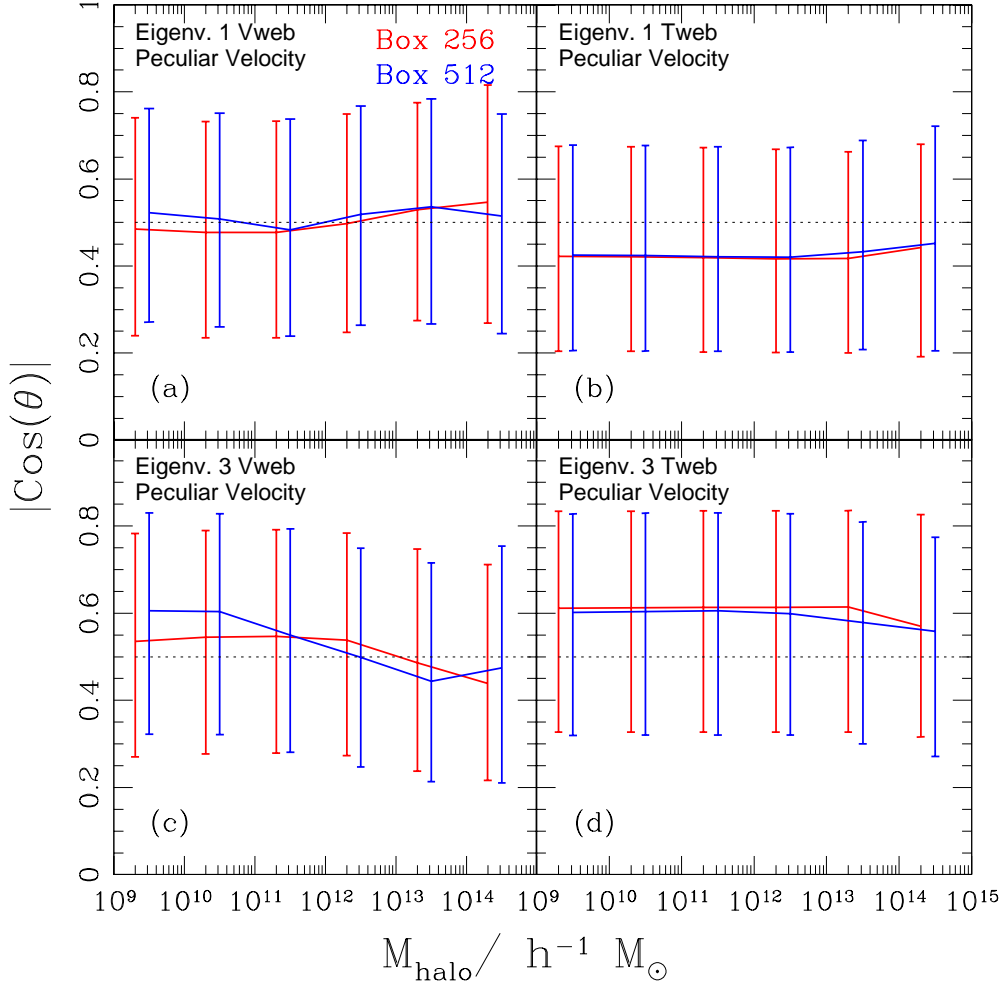


Figure 4. Median of $|\cos \theta|$ quantifying the peculiar velocity alignment with the Vweb (left) and the Tweb (right) for two different grid resolutions as a function of halo mass. In the upper (lower) panels the angle θ is measured between the first (third) eigenvector and a halo’s peculiar velocity.

web. The second method measures the average value of the angle between an eigenvector and the quantity of interest. These two measurements give us a complete picture for the different degrees of alignment in the web.

We find that the strongest alignment occurs for the halo shape with respect to the Tweb. In this case the halos tend to align with the third eigenvector, \hat{e}_3 , meaning that they lie along filaments and walls. This trend gets stronger as the halo mass increases and agrees with all the results published so far. Instead, for the momentum based Vweb, there is only an anti-alignment for halos more massive than $10^{12} h^{-1} M_\odot$, a result that is presented here for the first time.

A much weaker alignment signal is present for the angular momentum. In the Tweb only the most massive halos $> 10^{12} h^{-1} M_\odot$ are perpendicular with respect to \hat{e}_3 (anti-aligned to filaments), while for the Vweb the massive halos are aligned with \hat{e}_2 , lying along sheets. These results broadly agree with the published literature. Nevertheless, in some publications (Aragón-Calvo et al. 2007; Hahn et al. 2007; Aragón-Calvo & Yang 2014) there is an alignment signal reported at lower halo masses $< 10^{12} h^{-1} M_\odot$ that we do not detect in our measurements. One possible explanation for

this discrepancy can be appreciated by carefully looking at the results for different resolutions. The 512^3 grid does show a small anti-alignment for low mass haloes indicating that this signal could be related to scales smaller than $1 h^{-1} \text{Mpc}$. This would be consistent with (Paz et al. 2008), where using a different technique, they find an alignment for low mass haloes with the structure on small scales, and an anti-alignment at large scales (the 2-halo term). The diversity of results for the could be then interpreted as a high sensitivity of the alignment signal to the small scale cosmic web description, including numerical choices as to how interpolate the relevant fields.

A new result from our study is the alignment for the peculiar velocities. Here we find a relatively strong signal of alignment along the direction defined by the third eigenvector, \hat{e}_3 , and perpendicular to the first, \hat{e}_1 . This signal is clear in the Tweb for all masses below $< 10^{13} h^{-1} M_\odot$. This can be interpreted as a flow parallel to walls and filaments. In the case of the Vweb similar signal, albeit weaker, is present only for the low mass halos $< 10^{12} h^{-1} M_\odot$. A similar result was obtained by (Padilla et al. 2005) who found that pe-



Figure 5. Median of the $|\cos\theta|$ for the shape alignment of the major axis with the third eigenvector. Each panel shows different subsamples according to selections on five different properties: circularity, concentration, halo inner density, spin and triaxiality. Each subsets includes 30% of halos in the lower/higher end of each property. The grey band indicates the region around $|\cos\theta| = 0.5$ that indicates the absence of alignment.

culiar velocities are larger in the direction parallel to void walls.

The different behaviour for the alignments of massive halos in the Tweb and the Vweb is explained by an anti-alignment between the eigenvectors in the two web grids for massive halos $> 10^{12} h^{-1} M_{\odot}$. For low mass halos the directions defined by the two webs point in the same direction. This trends can be interpreted as non-linear effects that appear in the two different physical descriptions for the cosmic web, but the impact of the numerical choices to build the interpolation must be studied as well.

We also performed a simple study to find evidence of halo properties, other than mass, in driving the alignments. We find that in the case of shape, high concentration halos

or halos with a low value of the reduced spin parameter tend to show a stronger signal. This trend is more pronounced in the Tweb than in the Vweb. Concerning angular momentum we find that the anti-alignment signal is stronger for halos with high spin values. In the peculiar velocities we do not find any effect in the Tweb alignments, and the results for the Vweb show wide variations with grid resolution that impedes driving any strong conclusion.

Our study has shown that the alignment properties of dark matter halos depend on the physical definition of the cosmic web. This shows that the main aspect of non-linear gravitational collapse might be revealed easily depending on the choice of the physical context (i.e. tidal field vs. velocity shear). There is not a better method, but different perspec-

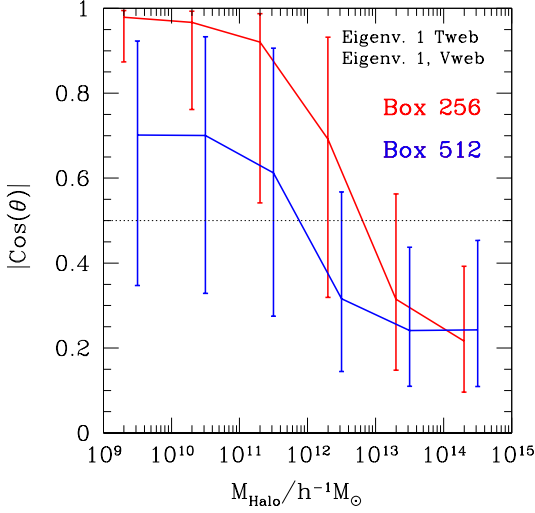


Figure 6. Median of the interweb alignment for the two grid resolutions as a function of the dark matter mass corresponding to the halos where the measurement was made. The error bars indicate the lower and upper quartiles.

tives. In future work we will explore the potential of these two complementary techniques in understanding the environmental dependence of galaxy evolution.

ACKNOWLEDGMENTS

J.E.F-R acknowledges the financial support by Vicerrectoría de Investigaciones at Universidad de los Andes through a FAPA grant. NP acknowledges support by Fondecyt Regular No. 1110328 and BASAL PFB-06 "Centro de Astronomía y Tecnologías Afines". NP and SC acknowledge support by the European Commissions Framework Programme 7, through the Marie Curie International Research Staff Exchange Scheme LACEGAL (PIRSES-GA-2010-269264). NP thanks the hospitality of the Max Planck Institute for Astrophysics at Garching during his sabbatical year 2013-2014. The Geryon cluster at the Centro de Astro-Ingeniería UC was extensively used for the calculations performed in this paper. The Anillo ACT-86, FONDECUIP AIC-57, and QUIMAL 130008 provided funding for several improvements to the Geryon cluster.

We thank the referee, Miguel Aragon-Calvo, for a constructive report that help us to improve the paper.

APPENDIX A. DETAILED DESCRIPTION OF PREVIOUS THEORETICAL RESULTS

In this Appendix we review the results that use a similar exploration techniques for halo alignments with the cosmic web. Other kind of alignment statistics based on modifications of the correlation (e.g. Paz et al. 2008; Faltenbacher et al. 2009) that go beyond a local computation and are not reviewed here.

- Libeskind et al. (2013)

They study the shape and angular momentum alignments with the cosmic web defined by the velocity shear

tensor method described in this paper. Libeskind et al. (2013) used the Bolshoi simulation and the halo catalogs we use in this work. Results are reported for three mass bins $M_{\text{vir}} < 10^{11.5} h^{-1} M_{\odot}$, $11^{11.5} < M_{\text{vir}} < 12^{12.5} h^{-1} M_{\odot}$ and $M_{\text{vir}} > 12^{12.5} h^{-1} M_{\odot}$. The identification of the cosmic web is done on a grid of 256^3 with a gaussian smoothing of $\sim 1 h^{-1} \text{Mpc}$ over the velocity field. The way they compute this smoothed velocity field differs from our computation. We do it based on the momentum density field while they do not take into account the mass in each cell.

The alignment signal for the angular momentum is weak while the shape alignment signal is very strong. The shape alignment is such that the eigenvector corresponding to the smallest eigenvalue is aligned with the major axis. This effect is stronger for more massive halos. In other words the major axis of a halo is aligned with a filament, and lies on the plane that define a sheet. The angular momentum is anti-aligned with the filament for massive halos and weakly aligned for low mass halos.

- Trowland et al. (2013)

They used the Millennium Run, which has 2160^3 particles in a volume of $500 h^{-1} \text{Mpc}$ on a side. This corresponds to a particle mass of $8.6 \times 10^8 h^{-1} M_{\odot}$. The catalog uses both halos and subhalos identified with SUBFIND. Only halos with more than 500 particles were kept to get a robust computation for the spin. The angular momentum is defined as the sum of the angular momentum of each particle with respect to the center of mass.

The method to define the filamentary structure is based on the eigenvalues of the hessian of the density. However, the analysis is performed on a box of $300 h^{-1} \text{Mpc}$ on a side. Four different gaussian smoothing scales are used: 2.0, 3.0 and $5.0 h^{-1} \text{Mpc}$.

By fitting the following functional form to the $\cos(\theta)$ distribution

$$P(\cos \theta) = (1 - c) \sqrt{1 + \frac{c}{2}} \left[1 - c \left(1 - \frac{3}{2} \cos^2 \theta \right) \right]^{-3/2}, \quad (6)$$

they are able to quantify the degree of alignment ($c < 0$) or anti-alignment ($c > 0$). This parameterization is based on theoretical expectations of Tidal Torque Theory (TTT) (Lee et al. 2005). At $z = 0$, the reported value is $c = 0.035 \pm 0.004$, where the uncertainty was calculated using bootstrapping and resampling.

When the halo sample is divided between low mass and high mass halos with a transition scale $M_{\star} = 5.9 \times 10^{12} M_{\odot}$, there is a weak alignment signal of the angular momentum against the principal filament axis for halos above that mass, for halos below that scale there is a weak anti-alignment.

- Codis et al. (2012)

They studies the alignment of the angular momentum dark relative to the surrounding large scale structure and to the tidal tensor eigenvalues.

They use a dark matter simulation with 4096^3 DM particles in a cubic periodic box of $2000 h^{-1} \text{Mpc}$ on a side, which corresponds to a particle mass of $7.7 \times 10^9 M_{\odot}$. Halos are identified using a FoF algorithm with a linking length of 0.2 keeping all halos with more than 40 particles, which sets the minimum halo mass to be $3 \times 10^{11} M_{\odot}$. In their work the particles were sampled on a 2048^3 grid and the density field was smoothed with a gaussian filter over a scale of

$5h^{-1}\text{Mpc}$ corresponding to a mass of 1.9×10^{14} . The skeleton was computed over 6^3 overlapping subcubes and then reconnected.

The filament finder algorithm is based on Morse theory and defines a Skeleton to be the set of critical lines joining the maxima of the density field through saddle points following the gradient. They also compute the hessian of the potential over the smoothed density field to get their eigenvectors.

The angular momentum of the halo is defined as $m_p \sum_i (r_i - \bar{r}) \times (v_i - \bar{v})$ where \bar{r} is the center of mass of the halo and \bar{v} is the average velocity.

They measure the alignment with each one of the eigenvectors. With respect to the minor eigenvector \bar{e}_3 (the filament direction) there is anti-alignment for masses $M > 5 \times 10^{12} M_\odot$ and alignment for masses $< 5 \times 10^{12} M_\odot$; with respect to the intermediate eigenvector \bar{e}_2 there is a strong alignment at high masses and no alignment for low masses; with respect to the major eigenvector \bar{e}_1 (normal to the wall plane) there is an anti-alignment signal at all masses. The results from the Skeleton algorithm are in agreement with the results from the Tidal web. The transitional mass is weakly dependent on the smoothing scale, varying between $1 - 5 \times 10^{12} h^{-1} M_\odot$ for smoothing scales between $1.0 - 5.0 h^{-1} \text{Mpc}$.

- (Zhang et al. 2009)

They studied the angular momentum and shape alignment against filaments. They used a dark matter simulation with 1024^3 DM particles in a periodic box of $100 h^{-1} \text{Mpc}$ on a side. The particle mass is $6.92 \times 10^7 h^{-1} M_\odot$. Dark matter haloes are found using a FOF algorithm with a linking length of 0.2 times the interparticle distance. Only halos with more than 500 particles are retained for further analysis. The angular momentum is measured with positions respect to the center of mass and the shape is determined using the non-normalized moment of inertia tensor.

The environment is found using the hessian of the density. The density field was interpolated over a 1024^3 grid and then smoothed with a Gaussian filter of scale $R_s = 2.1 h^{-1} \text{Mpc}$. There are two methods to define the direction of a filament. The first method uses the eigenvalues of the hessian density; they take the filament direction to be the eigenvector corresponding the single positive eigenvalue of the hessian. The second method used a line that connects the two terminal halos in a filament segment.

For the method that uses the eigenvectors, they find that the strength of the angular momentum alignment decreases with halo mass. For the shape they study the alignment of the major axis with the filament. They find an alignment signal in all mass bins, with an stronger effect for more massive halos.

In a final experiment they measure the angular momentum alignment in four different samples split by the strength of the shape alignment. They find that halos anti-aligned in shape, show a strong angular momentum correlation; and a strong angular momentum anti-alignment for halos with a strong shape alignment.

- (Aragón-Calvo et al. 2007)

They used the Multi-Scale Morphology Filter to describe the filamentary structure. The method is based on the Hessian matrix of the density field, which is computed from the particle distribution using a Delaunay tessellation field

estimator (DTFE). This allows them to identify clusters, filaments and walls.

They used a simulation with 512^3 particles in a cubic box of $150 h^{-1} \text{Mpc}$. The mass per particle is $2 \times 10^9 h^{-1} M_\odot$. Halo identification is done with the HOP algorithm. They keep halos with more than 50 particles and less than 5000, defining a mass range of $1 - 100 \times 10^{11} h^{-1} M_\odot$. The principal axes of each halo are computed from the non-normalized inertia tensor. The inertia tensor and the angular momentum are computed with respect to the center of mass of the halo.

They compute two angles, one with respect to the direction defining the filaments and the other the walls. Their results make a distinction between halos of more massive and less massive than $10^{12} h^{-1} M_\odot$. The angular momentum tends to lie along the plane of the wall, with a stronger alignment for massive halos. The effect for filaments is weaker, low mass halos tend to align along the filament, while high mass halos tend to be anti-aligned.

For the shape they find a very strong alignment along filaments. In walls the major axis lies along the wall. Both alignments are stronger for massive halos.

- (Hahn et al. 2007)

They used the hessian of the gravitational potential² applied on three simulations each of 512^3 particles, with sizes $L_1 = 45 h^{-1} \text{Mpc}$, $L_2 = 90 h^{-1} \text{Mpc}$ and $L_3 = 180 h^{-1} \text{Mpc}$, this corresponds to particle masses of 4.7, 38.0, $300 \times 10^7 h^{-1} M_\odot$. Halo identification was done with a FOF algorithm with 0.2 times the interparticle distance. They considered halos of at least 300 particles.

The web is obtained for a grid of 1024^3 cells, the density field is obtained with a CIC interpolation and smoothed using a Gaussian Kernel. All the results correspond to a smoothing scale of $R_s = 2.1 h^{-1} \text{Mpc}$.

They report on the angle between the halo angular momentum vector and the eigenvector corresponding to perpendicular directions to the sheets and the direction of the filaments. This is divided into two halo populations according to mass; low mass $5 \times 10^{10} - 1.0 \times 10^{12}$ and high mass $> 10^{12}$. They find a weak anti-alignment for filaments and a stronger anti-alignment in the case of the sheets. For the sheets the effect is stronger for the massive bin. The anti-alignment along filaments is weak regardless of the mass. They do not report any other significant statistic, but recognize that they suffer from small-number statistics in voids.

REFERENCES

- Abbas U., Sheth R. K., 2006, MNRAS, 372, 1749
- Aragón-Calvo M. A., van de Weygaert R., Jones B. J. T., van der Hulst J. M., 2007, ApJL, 655, L5
- Aragón-Calvo M. A., Yang L. F., 2014, MNRAS, 440, L46
- Baldry I. K., Balogh M. L., Bower R. G., Glazebrook K., Nichol R. C., Bamford S. P., Budavari T., 2006, MNRAS, 373, 469
- Bond J. R., Kofman L., Pogossyan D., 1996, Nature, 380, 603
- Codis S., Pichon C., Devriendt J., Slyz A., Pogossyan D., Dubois Y., Sousbie T., 2012, MNRAS, 427, 3320

² In (Hahn et al. 2007) the authors use a definition of the tidal field tensor equivalent with the T-Web method

- Colberg J. M., Krughoff K. S., Connolly A. J., 2005, *MNRAS*, 359, 272
- Courtois H. M., Hoffman Y., Tully R. B., Gottlöber S., 2012, *ApJ*, 744, 43
- Dekel A., Birnboim Y., Engel G., Freundlich J., Goerdt T., Mumcuoglu M., Neistein E., Pichon C., Teyssier R., Zinger E., 2009, *Nature*, 457, 451
- Dressler A., 1980, *ApJ*, 236, 351
- Dunkley J., Komatsu E., Nolte M. R., Spergel D. N., Larson D., Hinshaw G., Page L., Bennett C. L., Gold B., Jarosik N., Weiland J. L., Halpern M., Hill R. S., Kogut A., Limon M., Meyer S. S., Tucker G. S., Wollack E., Wright E. L., 2009, *ApJS*, 180, 306
- Faltenbacher A., Li C., White S. D. M., Jing Y.-P., Shu-DeMao Wang J., 2009, *Research in Astronomy and Astrophysics*, 9, 41
- Forero-Romero J. E., Hoffman Y., Gottlöber S., Klypin A., Yepes G., 2009, *MNRAS*, 396, 1815
- Gao L., Springel V., White S. D. M., 2005, *MNRAS*, 363, L66
- Gómez P. L., Nichol R. C., Miller C. J., Balogh M. L., Goto T., Zabludoff A. I., Romer A. K., Bernardi M., Sheth R., Hopkins A. M., Castander F. J., Connolly A. J., Schneider D. P., Brinkmann J., Lamb D. Q., SubbaRao M., York D. G., 2003, *ApJ*, 584, 210
- González R. E., Padilla N. D., 2009, *MNRAS*, 397, 1498
- González R. E., Padilla N. D., 2010, *MNRAS*, 407, 1449
- Hahn O., Carollo C. M., Porciani C., Dekel A., 2007, *MNRAS*, 381, 41
- Hinshaw G., Larson D., Komatsu E., Spergel D. N., Bennett C. L., Dunkley J., Nolte M. R., Halpern M., Hill R. S., Odegard N., Page L., Smith K. M., 2013, *ApJS*, 208, 19
- Hoffman Y., Metuki O., Yepes G., Gottlöber S., Forero-Romero J. E., Libeskind N. I., Knebe A., 2012, *MNRAS*, 425, 2049
- Jones B. J. T., van de Weygaert R., Aragón-Calvo M. A., 2010, *MNRAS*, 408, 897
- Kauffmann G., White S. D. M., Heckman T. M., Ménard B., Brinchmann J., Charlot S., Tremonti C., Brinkmann J., 2004, *MNRAS*, 353, 713
- Klypin A. A., Trujillo-Gomez S., Primack J., 2011, *ApJ*, 740, 102
- Lacerna I., Padilla N., 2011, *MNRAS*, 412, 1283
- Lee J., Erdogdu P., 2007, *ApJ*, 671, 1248
- Lee J., Kang X., Jing Y. P., 2005, *ApJL*, 629, L5
- Lee J., Pen U.-L., 2002, *ApJL*, 567, L111
- Li Y., Mo H. J., Gao L., 2008, *MNRAS*, 389, 1419
- Libeskind N. I., Hoffman Y., Forero-Romero J., Gottlöber S., Knebe A., Steinmetz M., Klypin A., 2013, *MNRAS*, 428, 2489
- Muñoz-Cuartas J. C., Müller V., Forero-Romero J. E., 2011, *MNRAS*, 417, 1303
- Muldrew S. I., Croton D. J., Skibba R. A., Pearce F. R., Ann H. B., Baldry I. K., Brough S., Choi Y.-Y., Conselice C. J., Cowan N. B., Gallazzi A., Gray M. E., Grützbauch R., 2012, *MNRAS*, 419, 2670
- Noh Y., Cohn J. D., 2011, *MNRAS*, 413, 301
- Nusser A., Branchini E., Davis M., 2011, *ApJ*, 735, 77
- Ocvirk P., Pichon C., Teyssier R., 2008, *MNRAS*, 390, 1326
- Oemler Jr. A., 1974, *ApJ*, 194, 1
- O'Mill A. L., Padilla N., García Lambas D., 2008, *MNRAS*, 389, 1763
- Padilla N., Lambas D. G., González R., 2010, *MNRAS*, 409, 936
- Padilla N. D., Ceccarelli L., Lambas D. G., 2005, *MNRAS*, 363, 977
- Park C., Choi Y.-Y., Vogeley M. S., Gott III J. R., Blanton M. R., SDSS Collaboration 2007, *ApJ*, 658, 898
- Paz D. J., Sgró M. A., Merchán M., Padilla N., 2011, *MNRAS*, 414, 2029
- Paz D. J., Stasyszyn F., Padilla N. D., 2008, *MNRAS*, 389, 1127
- Pimbblet K. A., Smail I., Kodama T., Couch W. J., Edge A. C., Zabludoff A. I., O'Hely E., 2002, *MNRAS*, 331, 333
- Riebe K., Partl A. M., Enke H., Forero-Romero J., Gottlöber S., Klypin A., Lemson G., Prada F., Primack J. R., Steinmetz M., Turchaninov V., 2013, *Astronomische Nachrichten*, 334, 691
- Sousbie T., Pichon C., Courtois H., Colombi S., Novikov D., 2008, *ApJL*, 672, L1
- Tempel E., Stoica R. S., Martínez V. J., Liivamägi L. J., Castellan G., Saar E., 2014, *MNRAS*, 438, 3465
- Trowland H. E., Lewis G. F., Bland-Hawthorn J., 2013, *ApJ*, 762, 72
- Tully R. B., Courtois H. M., Dolphin A. E., Fisher J. R., Héraudeau P., Jacobs B. A., Karachentsev I. D., Makarov D., Makarova L., Mitronova S., Rizzi L., Shaya E. J., Sorce J. G., Wu P.-F., 2013, *AJ*, 146, 86
- Wang X., Szalay A., Aragón-Calvo M. A., Neyrinck M. C., Eyink G. L., 2013, *ArXiv e-prints*
- Wilman D. J., Zibetti S., Budavári T., 2010, *MNRAS*, 406, 1701
- Zhang Y., Yang X., Faltenbacher A., Springel V., Lin W., Wang H., 2009, *ApJ*, 706, 747